Physics of Fluids

Effect of gusty inflow on the jet-switching characteristics of a plunging foil

Cite as: Phys. Fluids **32**, 117105 (2020); https://doi.org/10.1063/5.0024084
Submitted: 04 August 2020 . Accepted: 27 October 2020 . Published Online: 12 November 2020

Dipanjan Majumdar, Chandan Bose, and Sunetra Sarkar

Physics of Fluids ARTICLE scitation.org/journal/phf

Effect of gusty inflow on the jet-switching characteristics of a plunging foil

Cite as: Phys. Fluids 32, 117105 (2020); doi: 10.1063/5.0024084
Submitted: 4 August 2020 • Accepted: 27 October 2020 •
Published Online: 12 November 2020

Dipanjan Majumdar,[1] Chandan Bose,[2] and Sunetra Sarkar[1,a)]

AFFILIATIONS

[1] Department of Aerospace Engineering, Indian Institute of Technology Madras, Chennai 600036, India
[2] Department of Aerospace and Mechanical Engineering, University of Liège, Liège 4000, Belgium

[a)] **Author to whom correspondence should be addressed:** sunetra.sarkar@gmail.com

ABSTRACT

The effect of stochastic inflow fluctuations on the jet-switching characteristics of a harmonically plunging elliptic foil at a low Reynolds number regime has been analyzed in the present study. The inflow fluctuations are generated by simulating an Ornstein–Uhlenbeck process—a stationary Gauss–Markov process—with a chosen correlation function. In the absence of fluctuations, quasi-periodic movement of the wake vortices plays a key role in bringing out jet-switching at $\kappa h \geq 1.5$. However, fluctuating inflow alters the organized arrangement of the vortex street even at a lower κh ($\kappa h = 1.0$), giving way to an advanced jet-switching onset. More frequent switching with a larger deflection angle is also observed at $\kappa h = 1.5$ as compared to the no fluctuation case. Effects of inflow timescales on the deflection angle and switching frequency of the wake are investigated by varying the input correlation-lengths. The underlying flow physics are investigated through a qualitative study of the near-field interactions as well as various quantitative measures derived from the unsteady flow-field.

I. INTRODUCTION

From the design perspective of modern-day Flapping Wing Micro Aerial Vehicles (FWMAVs) or Automated Underwater Vehicles (AUVs), understanding the unsteady flow-field around flapping foils remains an important area of research to date. The aero/hydro-dynamic performance of these flapping devices intrinsically depends on the associated flow dynamics and the wake patterns. These, in turn, are largely dictated by key kinematic parameters such as the amplitude (A) and frequency (f_e) of the flapping motion. A plethora of experimental and numerical studies on the unsteady flow dynamics and the resulting wake patterns behind flapping foils are available in the literature.[1,2] The lightweight FWMAVs, designed to be operated in urban or forest settings with low flight-speed, are likely to be subjected to inflow fluctuations, which can significantly alter their aerodynamic performance.[3,4] To this end, a proper understanding of the ensuing unsteady wake patterns is crucial for an efficient design of such flapping devices. However, a large section in the literature assumed either uniform inflow or quiescent flow conditions. Although there have been some attempts to investigate the changes in the aerodynamic load characteristics of flapping foils under harmonic gusts,[5–8] the unsteady wake patterns under randomly fluctuating inflows remain largely unexplored in the existing literature.

The maximum non-dimensional plunge velocity (κh), proportional to the Strouhal number (St_A), is often considered as a control parameter to classify the wake patterns of a pure-plunging foil. Under steady uniform inflow, a transition from the drag-producing Kármán wake to the thrust-producing reverse Kármán wake takes place beyond $\kappa h > 0.6$.[9–11] At higher ranges of κh ($\kappa h \approx 1.0$), a symmetry breaking bifurcation occurs in the trailing-wake, resulting in a deflected reverse Kármán street,[11–13] and the deflection direction (either upward or downward) is dictated by the initial direction of the airfoil motion.[14] The deflection angle increases with the increase in κh or Re.[14] However, for a constant plunge amplitude (h), the deflection angle initially increases with the increase in reduced frequency (κ) until $\kappa \approx 15$ beyond which the deflection angle gradually decreases with the increase in κ.[14] According to the established "vortex-dipole" model,[12] strong self-advection and difference in phase velocities between the consecutive vortices play crucial roles in decoupling the bipolar vortex structures of a deflected wake. A recent extended model[14] showed the difference between

phase velocities of "symmetry-breaking" and "symmetry-holding" vortex pairs in a system of three consecutive vortices to be the main reasons for wake deflection. At higher values of κh, a complete reversal of the deflection direction, independent of the initial direction of the airfoil motion, may take place repeatedly with time, and this has been reported as "jet-switching" in the literature.[10,15–17] Reversal of the deflection direction from the far-end of the wake has also been reported.[18] For low-amplitude, high-frequency flapping, jet-switching has been associated with the process of "exchange of partners" between two consecutive vortex couples through a "vortex pairing process."[18] Shedding of strong leading-edge vortices (LEVs) is largely absent and thus cannot play any significant role in switching. Hardly any studies that report jet-switching have attempted to investigate the underlying vortex interaction mechanisms. A proper understanding of such mechanisms behind jet-switching and spontaneous reversal of the deflection direction is yet to be achieved.

There is also a standing debate in the existing literature, concerning the timescales of switching. Heathcote and Gursul,[15] in their experiments under quiescent flow conditions, observed the switching to repeat in a quasi-periodic manner ($Re_f = fc^2/\nu = 16\,200$ and $St_A = \infty$) with a return period to be at least two orders of magnitude higher than the flapping period. The period of jet-switching was seen to decrease with an increase in the plunge amplitude and the Strouhal number. These are in contrast to the observations of Jones *et al.*[10] who reported the switching to be random ($Re = 5 \times 10^2$ to 5×10^4 and $\kappa h = 1.5$). Shinde and Arakeri[16] also reported the switching to take place in an aperiodic manner for a pitching foil in quiescent flow ($Re_f = fc^2/\nu = 3234$ and $St_A = \infty$). It is to be noted that no switching was captured in the inviscid simulations of Jones *et al.*,[10] which marks the importance of viscosity behind this. Considering the conjecture made by the authors[10] that the random perturbations present in the flow-field during experiments are instrumental in providing the trigger for switching, it is potentially an interesting problem to examine the effects of stochastic inputs on wake vortices and, in turn, on the onset and frequency of switching. It would also be interesting to study the effect of the timescales present in a stochastic input and the flapping motion on the interval between two consecutive switching events. Note that the probability of jet-switching happening at a low κh remains relatively low in the presence of a single frequency periodic input, whereas a stochastic input with its broadband frequency spectra can create a more favorable condition for jet-switching due to the interplay of multiple frequencies present in it. Although some of the recent studies have investigated the effect of gusty/noisy inflows on flapping foils, the main focus was on examining the alterations in the aerodynamic load characteristics; the changes in vortex interactions or wake patterns were not explored. In most of the cases, the gust was considered to be a single frequency harmonic input[5–7] or a single frequency harmonic input with a spatial gradient.[8] However, stochastic inlet velocity is a more realistic approximation of the real life situation, compared to a periodic fluctuation.

In the present study, the flow-field around a harmonically plunging elliptic foil under fluctuating inflow is simulated using a discrete forcing type immersed boundary method (IBM)[19]-based in-house Navier–Stokes (N–S) solver[20] in the low Reynolds number regime ($Re = 300$). The input fluctuations are modeled as a stochastic process with two distinctly different orders of timescales and undertake an investigation of its role in facilitating the jet-switching phenomenon and in altering the parametric boundaries for qualitative changes in the wake. The dynamics of the trailing-wake at two different κh regimes, representing two qualitatively different dynamical states, are investigated. The specific objectives of the present study are the following: (i) to identify the mutual interactions among the near-field vortices and other key mechanisms that initiate deflection and jet-switching in the wake and (ii) to investigate the effect of stochastic inflow on the wake patterns and the onset of jet-switching, in comparison to the deterministic scenario. The organization of rest of this paper is as follows: computational methodology and the simulation setups are described in Sec. II; different quantitative measures to characterize the flow-field are given in Sec. III. Section IV describes the wake patterns at different κh for steady inflow, while the effects of input fluctuations are discussed in Sec. V; the associated vortex interaction mechanisms are given in Sec. VI. The salient outcomes are given in Sec. VII.

II. COMPUTATIONAL METHODOLOGY

A. Governing equations

A two-dimensional (2D) elliptic foil with a thickness to chord ratio of 0.12 is considered to exhibit a prescribed harmonic plunge motion. The kinematic equation describing the motion of the rigid foil is given in the non-dimensional form below,

$$\tilde{y}_c(\tilde{t}) = h\sin(\kappa\tilde{t}), \qquad \dot{\tilde{y}}_c(\tilde{t}) = \kappa h\cos(\kappa\tilde{t}). \tag{1}$$

Here, h $(=A/c)$, κ $(=2\pi f_e c/U_\infty)$, and $\tilde{t}$ $(=\frac{tU_\infty}{c})$ are the non-dimensional plunge amplitude, reduced frequency, and non-dimensional time, respectively, where U_∞ is the mean free-stream velocity and c is the chord-length of the foil.

The present work is focused in the low Reynolds number ($Re = \frac{U_\infty c}{\nu}$, with ν being the kinematic viscosity of the fluid) regime where the viscous effects are dominant. The flow around the plunging foil is governed by the 2D incompressible N–S equation as follows:

$$\frac{\partial\tilde{\mathbf{u}}}{\partial\tilde{t}} + \tilde{\nabla}\cdot(\tilde{\mathbf{u}}\tilde{\mathbf{u}}) = -\tilde{\nabla}\tilde{p} + \frac{1}{Re}\tilde{\nabla}^2\tilde{\mathbf{u}}, \tag{2}$$

$$\tilde{\nabla}\cdot\tilde{\mathbf{u}} = 0, \tag{3}$$

where $\tilde{\mathbf{u}} = \frac{\mathbf{u}}{U_\infty}$ and $\tilde{p} = \frac{p}{\rho_f U_\infty^2}$ (ρ_f denotes the fluid density) are the non-dimensional flow velocity and non-dimensional pressure, respectively. Although the entire discussion in the study is made in terms of non-dimensional quantities, the overbar sign ($\bar{}$) will be dropped hereafter for typographical ease. In addition, the time values in all these figures presented in this study are normalized by the time period of flapping, $T(=2\pi/\kappa)$. The fluid dynamic load coefficients (C_L and C_D) are defined as

$$C_L = \frac{L}{\frac{1}{2}\rho_f U_\infty^2 c} \quad and \quad C_D = \frac{D}{\frac{1}{2}\rho_f U_\infty^2 c}, \tag{4}$$

where L denotes the lift force (considered positive vertically upward along the y-axis) and D is the drag force (considered positive along the x-axis).

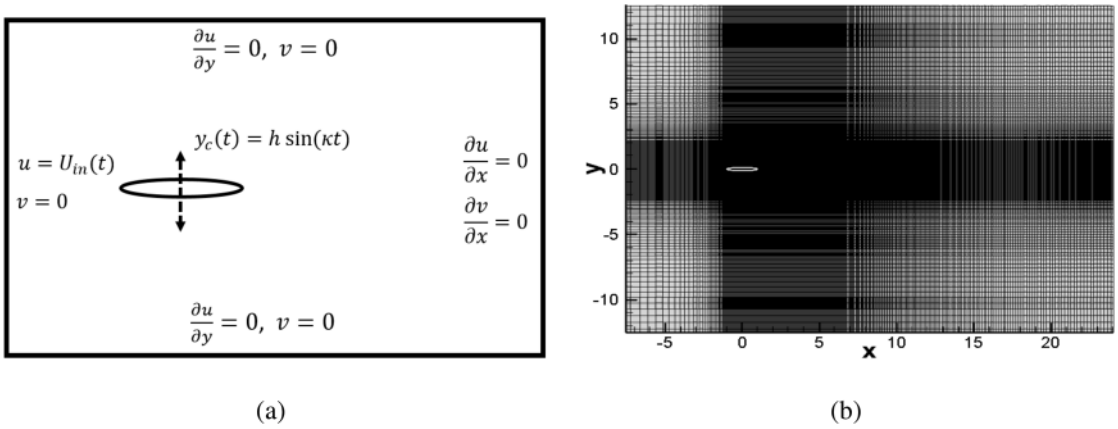

FIG. 1. (a) Schematic of the computational domain and (b) structured non-uniform mesh used in the present study.

B. Numerical solver

The flow governing equations are solved using an in-house discrete direct forcing type IBM solver.[20] The N–S equations are solved on a background Eulerian grid with the primitive flow variables being arranged in a staggered manner, while the movement of the plunging foil is tracked by a set of Lagrangian markers. The presence of the solid body inside the fluid domain is incorporated in the flow simulation by adding a forcing term to the momentum conservation equation. The momentum forcing reconstructs the velocity field at all the grid points inside the solid domain. It was shown in our earlier study[20] that this strategy ensures the no slip-no penetration conditions on the solid boundary with excellent accuracy. In addition, a source/sink term is added in the continuity equation to ensure rigorous mass conservation that reduces the pressure and velocity discontinuities across the immersed boundary. A finite volume-based semi-implicit fractional step method is implemented to perform the time marching. The convection term is advanced using the Adams–Bashforth technique, while the diffusion term is discretized according to the second order Crank–Nicolson method. Further details of the flow solver are available in our earlier study.[20] Different inflow cases are simulated in the present study by modifying the velocity boundary condition at the inlet of the computational domain, as demonstrated in Subsection II C.

A schematic view of the rectangular computational domain and the structured Cartesian mesh used in the present work are shown in Fig. 1. The size of the computational domain is selected through a domain independence test. It is set to be $[-10c, 25c] \times [-12.5c, 12.5c]$ to ensure that the aerodynamic loads on the plunging foil are insensitive to further increase in the domain size. A uniform grid spacing with the minimum grid size of $\Delta x \times \Delta y$ is considered in the region of the body movement. Outside this region, the grid size gradually increases as shown in Fig. 1(b). A minimum grid size of $\Delta x = \Delta y = 0.004$ has been chosen for all the simulations presented in this study, also $\Delta t = 0.0001$ is taken as the appropriate time-step size. For time and grid convergence studies as well as a thorough validation of the present IBM solver, see Ref. 20); these are not been presented here for the sake of brevity.

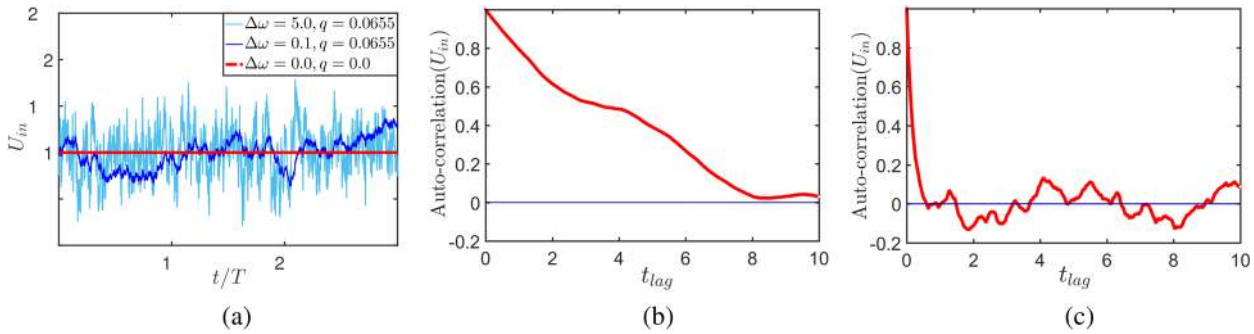

FIG. 2. (a) Time evolution of the inlet fluctuation in the stream-wise direction; auto-correlation of the fluctuating inlet velocities: (b) long time-scaled input and (c) short time-scaled input.

TABLE I. Parameter space.

Parameters	Values
Reynolds number	$Re = 300$
Reduced frequency	$\kappa = 4.0$
Non-dimensional plunge amplitude	$h = 0.25$ and 0.375
Constant inflow	$\Delta\omega = 0.0$, $q = 0.0$
Long time-scaled input	$\Delta\omega = 0.1$, $q = 0.0655$
Short time-scaled input	$\Delta\omega = 5.0$, $q = 0.0655$

C. Implementation of inlet boundary condition for stochastic inputs

Three different inlet boundary conditions have been considered in this study: (a) a steady uniform free-stream, (b) stochastic inflow with long timescales (significantly larger than the flapping timescale), and (c) stochastic inflow with short timescales (comparable to the flapping timescale). The stream-wise stochastically fluctuating inflows require an unsteady inlet boundary condition. Dirichlet type boundary conditions of $u = U_{in}(t)$ and $v = 0$ are considered at the inlet of the computational domain; no transverse fluctuation and spatial variation have been considered. At every time step, the corresponding value of the inlet velocity is supplied to the flow solver. At the top and bottom boundaries of the computational domain, a slip boundary condition ($\partial u/\partial y = 0$, $v = 0$) is used and a Neumann type boundary condition ($\partial \mathbf{u}/\partial x = 0$) is implemented at the outlet.

The unsteady flow velocity $U_{in}(t)$ is evaluated as

$$U_{in}(t) = U_\infty + u'(t), \tag{5}$$

where U_∞ is the deterministic mean flow component of the velocity and $u'(t)$ denotes the unsteady random fluctuation, $u'(t)$ is mathematically modeled as the Ornstein–Uhlenbeck (O–U) stochastic process,[21,22] chosen here because of its wide applications in various physical problems. The O–U process—a stationary Gauss–Markov process—is defined by the following stochastic differential equation:

$$du'(t) = -\Delta\omega u'(t)dt + \sqrt{2\Delta\omega q}\, dW(t), \tag{6}$$

where $W(t)$ is a Wiener process and $\Delta\omega$ and q are the noise parameters determining the timescale and variance, respectively. The correlation function of the O–U process is given by

$$\rho(t) = \langle u'(t)u(0)\rangle = qe^{-\Delta\omega|t|}. \tag{7}$$

Each realization of the O–U process is computed by numerically integrating the stochastic differential equation [Eq. (6)] using the Euler–Maruyama method.[23]

The correlation of the O–U noise is varied by varying the parameter $\Delta\omega$; two different $\Delta\omega$ values of 0.1 and 5.0 have been considered here, keeping q to be constant at 0.0655, to establish two different orders of timescales for the input fluctuations. Figure 2(a) shows the typical realizations of the random inlet velocity [$U_{in}(t)$] obtained from the chosen parameters. In this figure, the red-dashed line, denoted by $\Delta\omega = 0.0$ and $q = 0.0$, depicts the velocity for the deterministic case. The auto-correlation of $U_{in}(t)$ for the two random cases is presented in Figs. 2(b) and 2(c), respectively. It can be seen that as $\Delta\omega$ is increased from 0.1 to 5.0, the correlation length of the process decreases significantly. The correlation length with $\Delta\omega = 5.0$ is of the same order as the plunging period of the foil and will be called the short time-scaled input hereafter. Whereas the correlation length with $\Delta\omega = 0.1$ is much higher compared to the plunging time period and will be referred to as the long time-scaled input in the present study.

In order to capture the different flow patterns of interest, simulation results are presented for two different h values keeping κ constant, which results in two non-dimensional plunge velocity regimes, $\kappa h = 1.0$ and 1.5. Three different inflow conditions have been considered as mentioned earlier. The Reynolds number is assumed to be fixed at $Re = 300$. Table I summarizes the parameter space considered in the present study.

III. QUANTITATIVE MEASURES TO COMPARE DETERMINISTIC AND STOCHASTIC CASES

The trailing-wakes have been characterized quantitatively by defining a wake deflection angle, θ, which is a measure of the trend of average deflection of the vortex street in the wake. The deflection angle (θ) along with the velocity magnitude contour at the end of a typical plunging cycle is shown in Fig. 3(a). In this figure, the purple circular markers denote the y-location of the maximum flow velocity at different stream-wise locations (within a range of $1c$ to $8.5c$ from the trailing-edge), and the blue dashed line depicts a linear fit of those points. The blue dashed-dotted line shows the mean

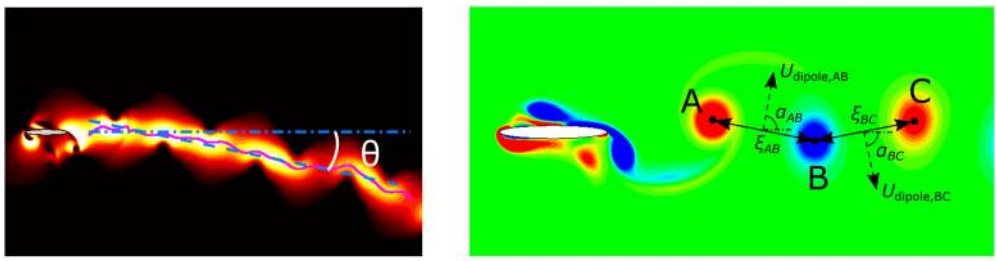

(a) (b)

FIG. 3. (a) Definition of the deflection angle (θ) and (b) schematic representation of the quantitative measures associated with vortex couples.

position of the plunging motion. The angle made by these two lines is defined as θ. A positive θ will be denoted as an upward deflected trailing-wake in this paper.

In the interest of the present study, the shift in the near-wake vortex locations and the distortion of the vortex streets under input fluctuations need to be captured and quantified. Earlier coined quantitative measures (*distance between vortices*, *circulation, and self-induced velocities of vortex pairs*)[12,14] are also employed in this study toward this requirement and are utilized to investigate the flow-interactions. Wei and Zheng[18] used a *cross-flow effective phase velocity*, V_p^*, of a couple to measure the ability of a vortex couple to escape the "symmetrizing" effect of the subsequent vortices in the wake. It is defined as

$$V_p^* = U_{\text{dipole}} \sin\alpha - V_{\text{phase}}, \tag{8}$$

where V_{phase} is the advection speed of a vortex couple in the cross-flow direction and α denotes the angle made by the direction of the self-induced velocity (U_{dipole}) of the couple with the streamwise direction, as shown in Fig. 3(b). U_{dipole} of a vortex couple is computed using the Biot–Savart law as given below,

$$U_{\text{dipole}} = \frac{\Gamma_{\text{avg}}}{2\pi\xi}, \tag{9}$$

where Γ_{avg} is the average absolute circulation of individual vortices in a vortex couple and ξ is the distance between them. Wei and Zheng[18] used this model to demonstrate that the difference in the U_{dipole} values can play a major role in dictating the direction of local deflection. The present study also utilizes these measures (ξ, Γ_{avg} and U_{dipole}) in order to quantify the effect of flow-fluctuations on jet-switching. The centers of the vortex cores in the near-wake are determined by performing a search of the local maxima and minima in the vorticity field, which are then used to evaluate the above quantities. The detailed procedure for calculating ξ and Γ_{avg} can be found in the study presented by Godoy-Diana *et al.*[12]

Refer to the schematic plot shown in Fig. 3(b), representing the near-field vorticity contour at the end of a typical plunging cycle. By definition, here, ξ_{AB} is the distance between the first counter-clockwise (CCW) vortex core **A** and the first clockwise (CW) core **B** present at the near-field; ξ_{BC} denotes the distance between **B** and the next CCW vortex core **C**. Similarly, Γ_{avg}^{AB} and Γ_{avg}^{BC} are the average circulations of the vortex couples **A**–**B** and **B**–**C**, respectively. As the flow-field evolves with time, if **B** comes closer to **A**, i.e., ξ_{AB} becomes lower than ξ_{BC}, then couple **A**–**B** dominates over **B**–**C**. As a result, **A**–**B** tries to deflect the mean flow toward the upward direction and influences the subsequent vortices to follow the upward same path. This scenario gets reversed when **B** gets closer to **C**. The dominance of a vortex couple over another is represented by its higher U_{dipole} than the other. Quantities such as dipole velocity ratio U_{dipole}-ratio ($=U_{\text{dipole}}^{AB}/U_{\text{dipole}}^{BC}$), distance ratio ξ-ratio ($=\xi_{AB}/\xi_{BC}$), and circulation ratio Γ_{avg}-ratio ($=\Gamma_{\text{avg}}^{AB}/\Gamma_{\text{avg}}^{BC}$) of the couples will be used to discuss their relative dominance. Since the couple of CCW vortex **A** and CW vortex **B** tries to deflect the wake in the upward direction [in the direction of their self-induced velocity as shown in Fig. 3(b)], couples such as **A**–**B** will be referred to as the upward deflecting couple. Whereas couples such as **B**–**C**, which tries to deflect the wake downward, will be referred to as the downward deflecting couples in this study. In a given situation, when the distances between the vortex cores of **A**–**B** and **B**–**C** are unequal, one of these couples will dominate and try to break the symmetry in the flow-field by deflecting the wake in the direction of its self-induced velocity; this dominant couple will be referred to as the symmetry-breaking couple in Secs. IV–VI.

IV. WAKE DEFLECTION AND JET-SWITCHING UNDER STEADY INFLOW

A. κh = 1.0 (onset of deflection)

The symmetry breaking bifurcation occurs at around $\kappa h \approx 1.0$,[11] where the reverse Kármán vortex street starts to deflect upward or downward depending on the initial direction of the airfoil motion. The corresponding C_D time history exhibits a periodic behavior, as shown in Fig. 4(a). The trailing-wake patterns in different cycles also match exactly, upholding the periodic signature. At this smaller plunge velocity, there is no strong LEV separation, and the flow remains attached with the foil. The staggered arrangement of the alternate CW and CCW shed vortices gives way to a stable reverse Kármán street with a mild upward deflection [see Fig. 4(b)]. At this lower κh, the deflection angle remains very small ($\leq 1^\circ$) in the chosen low *Re* regime, which is consistent with the work of Zheng and Wei.[14] In the trailing-wake, CW vortex **B** remains almost equidistant from the surrounding CCW vortices (**A** and **C**), and

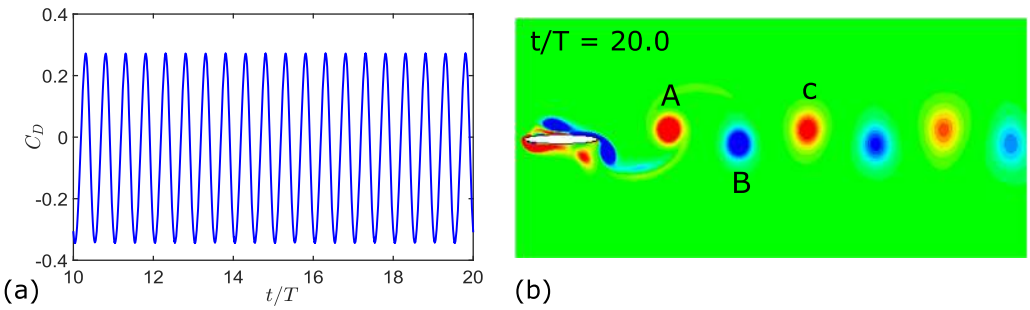

FIG. 4. At κh = 1.0, under constant inflow: (a) drag coefficient and (b) periodic reverse Kármán wake.

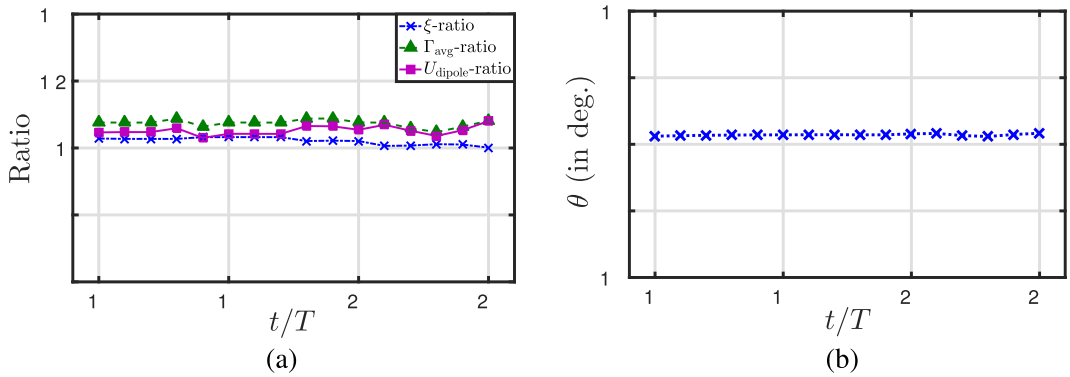

FIG. 5. At κh = 1.0, under constant inflow: (a) quantitative measures and (b) deflection angle. Dominant effect of the upward deflecting vortex couple **A**–**B** results in a positive deflection angle.

therefore, the ξ-ratio (distance ratio) remains nearly constant at 1.0 [Fig. 5(a)]. However, the circulation Γ_{avg}-ratio [Fig. 5(a)] takes values higher than unity, depicting a mild dominance of the upward deflecting couple **A**–**B** over **B**–**C**. This results in higher self-induced velocity for upward deflecting **A**–**B** [Fig. 5(a)], helping the mean jet of the wake to deflect in the upward direction. Since the difference between U^{AB}_{dipole} and U^{BC}_{dipole} is not significant, θ shows a small positive value that remains almost constant after the initial transients [see Fig. 5(b)]. Since the positions of the vortex cores do not get disturbed, and the distances between the cores do not change in

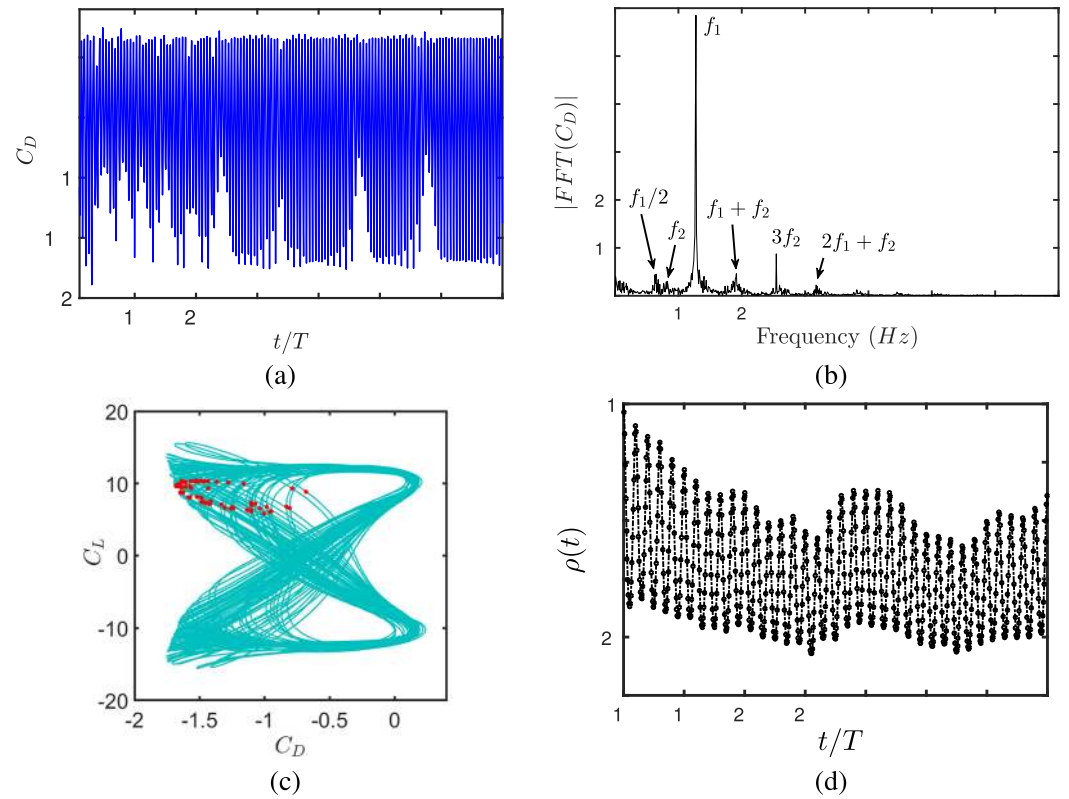

FIG. 6. At κh = 1.5, under constant inflow: (a) time-history of C_D, (b) frequency spectra, (c) C_L–C_D phase portrait and Poincaré section (red dots), and (d) correlation of the stream-wise velocity field with the reference velocity field at t_{ref}/T = 10.

different cycles, the same couple (**A**–**B**) remains dominant in every cycle. However, in a different simulation, depending on the initial direction of the plunge motion, one might observe couple **B**–**C** to be the dominant one, resulting in a downward deflected wake.

B. κh = 1.5 (jet-switching)

In this κh regime, a qualitatively different wake pattern and dynamics are observed compared to the earlier case. The C_D time-history [Fig. 6(a)] shows a modulating envelope with a net positive thrust. The corresponding frequency spectra [Fig. 6(b)] show the presence of two fundamental incommensurate frequencies f_1 and f_2, and the other peaks appear in a linear combination of these two, which is representative of quasi-periodic dynamics. The toroidal C_L–C_D phase-portrait [Fig. 6(c)] and a neat closed loop pattern in the Poincaré section [red dots in Fig. 6(c)] also confirm the quasi-periodic state.[24] These can be attributed to the fact that the state of a quasi-periodic system can never repeat exactly but can only traverse back to its close neighborhood in the phase-space. The correlation [$\rho(t)$ in Eq. (10)] time history of the stream-wise velocity field with respect to a reference instant of $t_{\text{ref}}/T = 10$ is seen to oscillate approximately between 0.15 and 0.75 [see Fig. 6(d)]. This indicates that the flow-pattern at different cycles neither repeat exactly nor is very different from each other, which is representative of quasi-periodicity,[20]

$$\rho(t) = \frac{\sum_{i,j=1}^{m,n}(u_{ij}(t) - \overline{u}(t))(u_{ij}(t_{\text{ref}}) - \overline{u}(t_{\text{ref}}))}{\sqrt{\sum_{i,j=1}^{m,n}(u_{ij}(t) - \overline{u}(t))^2}\sqrt{\sum_{i,j=1}^{m,n}(u_{ij}(t_{\text{ref}}) - \overline{u}(t_{\text{ref}}))^2}}. \quad (10)$$

Here, $\overline{u}$ is the spatial average of the stream-wise velocity within a chosen domain and m and n are the numbers of grid points along the x- and y-axis, respectively, within the domain of consideration.

The corresponding wake pattern shows a well deflected reverse Kármán street (Fig. 7) with varying angles of deflection from one cycle to another. Note that the magnitude of the deflection angle has increased with the increase in κh from 1.0 to 1.5. This is in good agreement with the literature.[14] In this case, the wake vortices do not repeat exactly in the consecutive cycles (unlike the case of κh = 1.0). Instead, their core positions shift marginally from cycle to cycle due to quasi-periodicity. The variation of the distances between the vortex cores is presented quantitatively in terms of the ξ-ratio in Fig. 8(a). The corresponding Γ_{avg}-ratio also shows variations from one cycle to another [see Fig. 8(a)]. Although the ξ-ratio remains close to unity during the initial stage, the Γ_{avg}-ratio displays values lower than 1.0. This results in a higher downward self-induced velocity for **B**–**C** compared to the upward deflecting couple **A**–**B**. This is substantiated by the U_{dipole}-ratio being lower than 1.0 [Fig. 8(a)]. Eventually, the dominant effect of **B**–**C** deflects the wake downward, depicted by negative θ values during the initial cycles [Fig. 8(b)]. The relative dominance slowly gets shifted from the downward deflecting couple **B**–**C** to the upward deflecting couple **A**–**B**. At the end of the 25th cycle, the U_{dipole}-ratio crosses unity [Fig. 8(a)], showing the dominance of **A**–**B** over **B**–**C**. However, this is happening locally in the near-field and therefore would not be reflected immediately in the θ value. As this dominant **A**–**B** convects downstream, it pulls the subsequent vortices to follow the upward deflected path. Consequently, the trailing-wake gradually deflects upward in the following cycles, and the entire

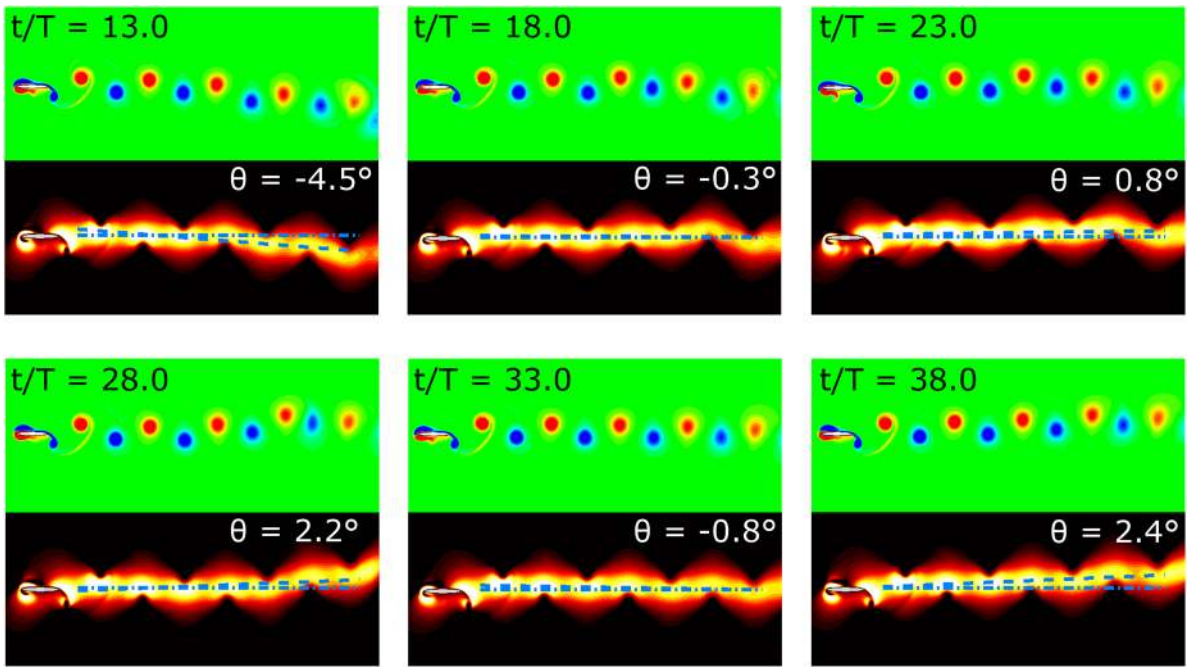

FIG. 7. At κh = 1.5, under constant inflow: instantaneous vorticity (top) and velocity (bottom) contours represent mildly deflected wake pattern undergoing jet-switching.

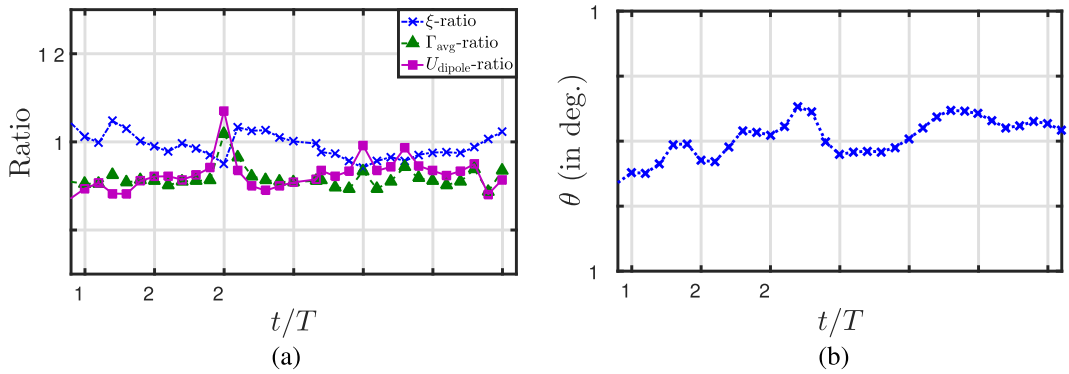

FIG. 8. At κh = 1.5, under constant inflow: (a) quantitative measures and (b) deflection angle. Alternate dominance of the upward and downward deflecting vortex couples results in jet-switching.

wake looks deflected upward with a high deflection angle as seen for θ at t/T = 27. As time progresses, the relative dominance once again shifts from **A**–**B** to **B**–**C**. Recall that for κh = 1.0 (periodic case), the same vortex couple (either **A**–**B** or **B**–**C**, depending on the initial direction of the plunge motion) remained dominant for all time. On the contrary, in the present case (quasi-periodic), the dominance switches alternately. As a result, the downward wake with $\theta = -4.5^\circ$ at t/T = 13.0 becomes upward deflected with $\theta = 2.2^\circ$ at t/T = 28.0; again, θ changes from -0.8° at t/T = 33.0 to 2.4° at t/T = 38.0, as shown in Fig. 8(b) (see also Fig. 7). Thus, quasi-periodicity, by bringing small changes in vortex strengths and core locations, plays the key role in the formation of upward or downward deflecting couples whose mutual competition triggers the alternate upward–downward deflection of the wake. The underlying mechanism remains similar to the vortex-pairing process, as reported in Ref. 18, and no significant interaction of LEV with the trailing-edge vortices (TEVs) is observed.

V. JET-SWITCHING UNDER STOCHASTIC INFLOWS OF DIFFERENT TIMESCALES

The effects of long and short time-scaled input fluctuations on the wake patterns at κh = 1.0 and 1.5 are investigated by changing the $\Delta\omega$ value in the O–U process [Eq. (6)]. Under fluctuating inflows, shifts in the vortex strengths and core locations can take place at κh values significantly lower than 1.5, giving rise to alternatively dominant upward and downward deflecting couples. This advances the jet-switching onset in the κh parametric space from that of the deterministic scenario. In addition, the movement of the near-wake vortices at higher κh values (κh = 1.5) gets much more energized in the presence of the input fluctuations. This helps in the formation of stronger symmetry breaking couples, resulting in complete reversals of the trailing-wake orientation accompanied by significantly larger deflection angles.

A. Effect of inflow fluctuation at κh = 1.0

Figure 9 compares the wake patterns in which the instantaneous vorticity contours at the end of three typical plunging cycles are presented. Recall that under the uniform inflow, an organized pattern of reverse-Kármán shape was observed, where CW **B** remained equidistant from CCW **A** and **C**. This gets disturbed under fluctuating inflows, and the distances between the vortex cores as well as their strengths change in a random fashion. While mild distortions are observed for the long time-scaled input [Fig. 9(b)], they become prominent under the short time-scaled case [Fig. 9(c)]. Especially for the latter, when two counter-rotating vortices come too close to each other, a strong symmetry-breaking couple is formed. It traverses with its self-induced velocity and pulls the fluid behind it, deflecting the wake in the direction of its movement. The dominant symmetry-breaking vortex couples are marked with dashed rectangular boxes in Fig. 9(c). Note the smaller distances between the vortex cores **A**–**B** at t/T = 20, **B**–**C** at t/T = 23, and **A**–**B** at t/T = 26. At t/T = 20, the strong upward deflecting couple **A**–**B** is formed in the near-wake. As this couple convects in the downstream, gradually the wake becomes upward deflected in the subsequent cycles until t/T = 23. However, at t/T = 23, the downward deflecting **B**–**C** becomes dominant. They pulled the subsequent vortices downward until a dominant upward deflecting couple is formed again. The associated velocity contours and the deflection angles under the short time-scaled case are presented in Fig. 10, clearly depicting jet-switching.

1. Advancement of the jet-switching onset

The variation of the wake deflection angle (θ) with time, under the three different inflow conditions, is shown in Fig. 11(a). In the presence of input fluctuations, θ fluctuates and changes its sign. This is indicative of "jet-switching" at the trailing-wake. As the position of the vortex cores in the trailing-wake repeats exactly under uniform flow, no switching or reversal in the deflection direction is observed. Under the long time-scaled fluctuations, though switching takes place, the deflection angles remain very small due to the minor distortions of the vortices. However, this becomes more prominent under the short time-scaled input. As also shown in Fig. 10, the wake deflection angle changes from negative to positive and vice versa. These results establish that input fluctuations can indeed advance

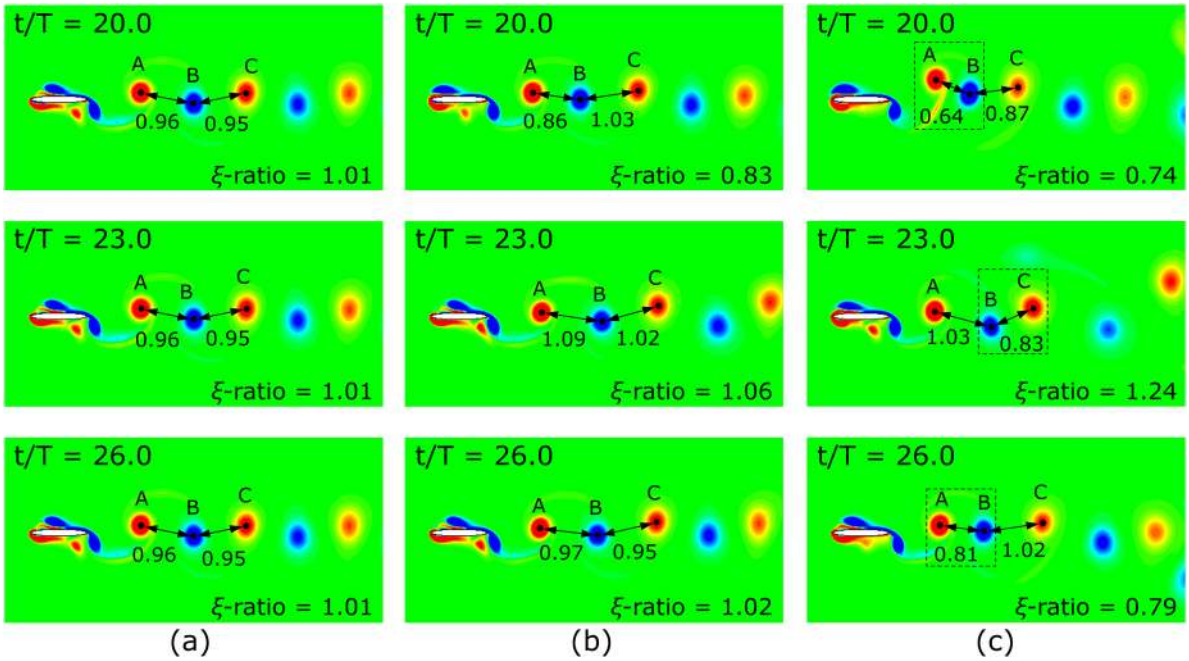

FIG. 9. At κh = 1.0, comparison of the trailing-wake patterns for (a) constant inflow, (b) long time-scaled input, and (c) short time-scaled input.

the onset of the jet-switching regime by affecting the movement of the vortices.

2. Mechanisms behind the advancement of jet-switching

In order to investigate the flow-field behavior that triggers the advancement, three immediate key vortices, **A**, **B**, and **C**, present in the trailing-wake (as shown in Fig. 9) are tracked for 20 consecutive cycles. The variation in the U_{dipole}-ratio, ξ-ratio, and Γ_{avg}-ratio of the couples is shown in Figs. 11(b), 11(c), and 11(d), respectively. Under the short time-scaled input, the ξ-ratio deviates significantly from unity. As the ξ-ratio becomes substantially lower than 1.0, e.g., at t/T = 20.0 in Fig. 11(c), **A** and **B** come really close, and **B** and **C** move far apart. CCW **A** and CW **B** form a couple. Consequently, U^{AB}_{dipole} increases to almost 150% of U^{BC}_{dipole} at that instant. The dominant effect of **A**–**B** starts pulling the wake upward even though the overall pattern looks downward [see Fig. 11(b)]. Eventually, the vortex street gets deflected upward in the following cycles [Figs. 10 and 11(a)]. The scenario reverses when the ξ-ratio becomes substantially higher than 1.0 [e.g., at t/T = 24.0 in Fig. 11(c)] and **B**–**C** forms a couple. Here, U^{AB}_{dipole} drops to 75% of U^{BC}_{dipole}, and the dominant effect of **B**–**C** starts pulling the whole wake downward. Eventually, the wake becomes downward in the following cycles [Figs. 10

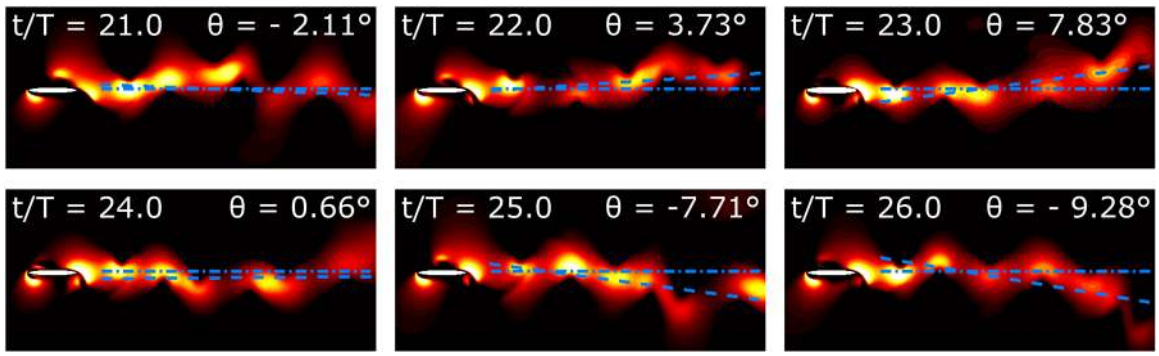

FIG. 10. At κh = 1.0, under the short time-scaled input: velocity contours and wake deflection angles at the end of six consecutive plunging cycles.

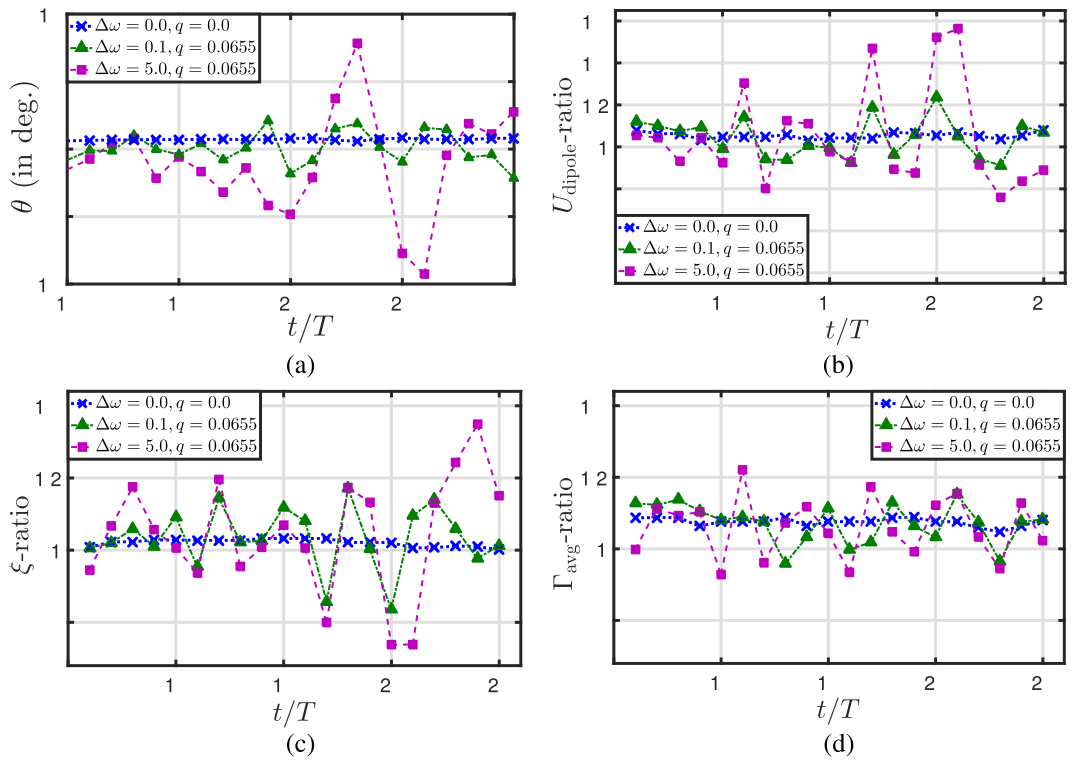

FIG. 11. At κh = 1.0, variation of (a) deflection angle, (b) dipole velocity ratio, (c) distance ratio, and (d) circulation ratio at the end of 20 consecutive plunging cycles for different inflow conditions.

and 11(a)]. Another important point that emerges from Fig. 11(d) is that the Γ_{avg} ratio is not as important as parameter the ξ-ratio, and the latter has a more dominant effect on the formation of the couples. The vortex core centers are plotted in Fig. 12. In contrast to the uniform input case [Fig. 12(a)], the positions of the vortex cores start to slightly deviate in different cycles as the long time-scaled fluctuation is introduced [Fig. 12(b)], and these deviations become quite significant in the presence of the short time-scaled input [Fig. 12(c)]. This is quantitatively demonstrated by estimating the variances of the scattered vortex-core centers. For the short time-scaled case, the

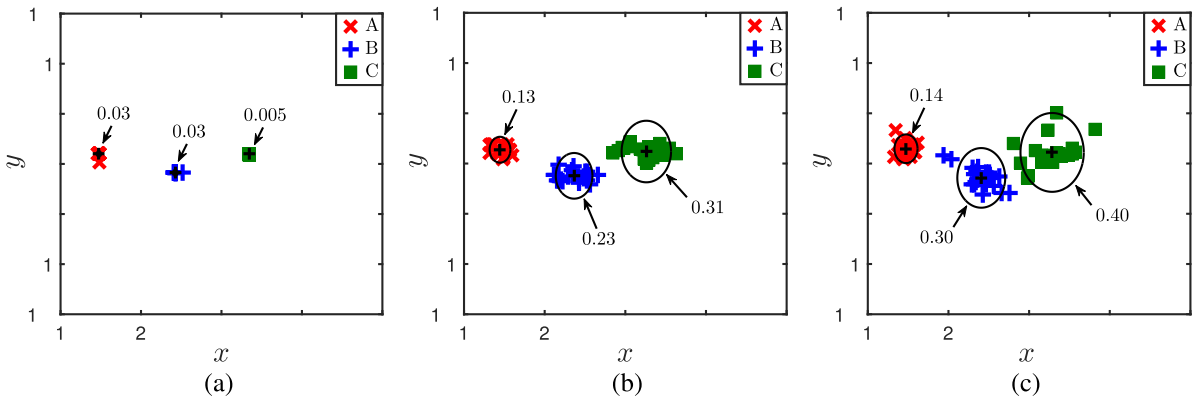

FIG. 12. At κh = 1.0, locations of the vortex core centers of **A**, **B**, and **C** at the end of 20 consecutive plunging cycles (from 6th to 25th) for (a) constant inflow, (b) long time-scaled input, and (c) short time-scaled input.

variance in the positions of **A**, **B**, and **C** increases to 0.14, 0.30, and 0.40, respectively, from the small near-zero values corresponding to the uniform inflow case. Thus, it is fairly conclusive that the perturbations introduced in the flow-field by the input fluctuations are the main instrument that triggers the wake vortices to deviate from their otherwise stable arrangement.

B. Effect of inflow fluctuation at κh = 1.50

The study of the effect of inflow fluctuations at this higher κh regime is more interesting, as a mild form of jet-switching was already observed at this κh under uniform inflow. The corresponding wake pattern undergoes a more frequent jet-switching with considerably higher deflection angles. This is demonstrated next.

1. Vigorous jet-switching with higher deflection angles

To see the effect of flow-fluctuations on the wake pattern, instantaneous vorticity contours at the end of two typical cycles are presented in Fig. 13. This demonstrates the presence of jet-switching with considerably higher deflection angles. The change in θ for five consecutive cycles is quantitatively presented in Fig. 14. In the presence of the long time-scaled input, the trailing-wake pattern [Figs. 13(b) and 14(b)] maintains an overall similarity to the uniform inflow case [Figs. 13(a) and 14(a)]. On the other hand, more vigorous wake reversals are visible under the short time-scaled input [see Figs. 13(c) and 14(c)]. At t/T = 16.0 and t/T = 23.0, **B**–**C** and **A**–**B**, respectively, act as the dominant symmetry-breaking couples in the already existing downward and upward deflected wakes. Thus, they help in increasing the angles of deflection further. The dominance of **A**–**B** and **B**–**C** gets interchanged in different cycles, giving way to switching. Note that only a few representative cycles are shown here for the sake of brevity. The complete temporal evolution of the wake can be seen from the supplementary material. The time evolution of θ, presented in Fig. 15(a), establishes quantitatively how weak jet-switching under uniform inflow changes to vigorous upward–downward transition of the wake, especially under the short time-scaled input. The short time-scaled fluctuation not only advances the switching onset but also enhances the deflection angles. Here, θ takes values as high as -23.3° at t/T = 18.0 during downward deflection and 21.0° at t/T = 43.0 during upward deflection [see Figs. 14(c) and 15(a)]. Furthermore, switching occurs much more frequently compared to the other two cases.

2. Explanations for vigorous switching

The ξ-ratio, U_{dipole}-ratio, and Γ_{avg}-ratio for couples **A**–**B** to **B**–**C** are presented in Figs. 15(c), 15(b), and 15(d), respectively, for 40 consecutive flapping cycles. Expectedly, these measures do not vary significantly and remain close to unity for both uniform and long time-scaled inflows. Significant fluctuation is visible in the case of short timescale. For example, at t/T = 16.0, the ξ-ratio is 1.55, signifying that **B**–**C** forms the dominant symmetry-breaking couple. Consequently, U^{AB}_{dipole} drops to 60% of U^{BC}_{dipole}, and the dominant effect of **B**–**C** pulls the wake downward. This scenario gets reversed at t/T = 21.0 when the ξ-ratio is 0.75, and the dominant effect of **A**–**B** pulls the wake upward. Similar role reversals continue to take place in the wake with time. The change in the Γ_{avg}-ratio also creates larger differences in the self-induced velocities, resulting in higher deflection angles.

The fluctuations in the ξ-ratio are seen to be much higher than those of the Γ_{dipole}-ratio, once again confirming that the change in the distances between the vortex cores eventually becomes the main

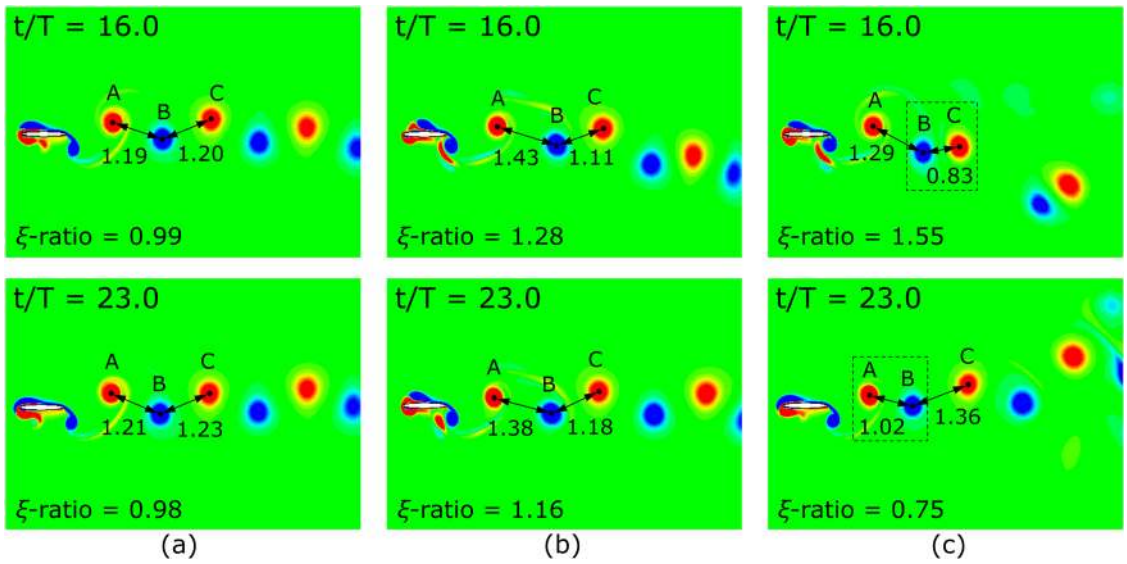

FIG. 13. At κh = 1.5, comparison of the trailing-wake patterns for (a) constant inflow, (b) long time-scaled input, and (c) short time-scaled input.

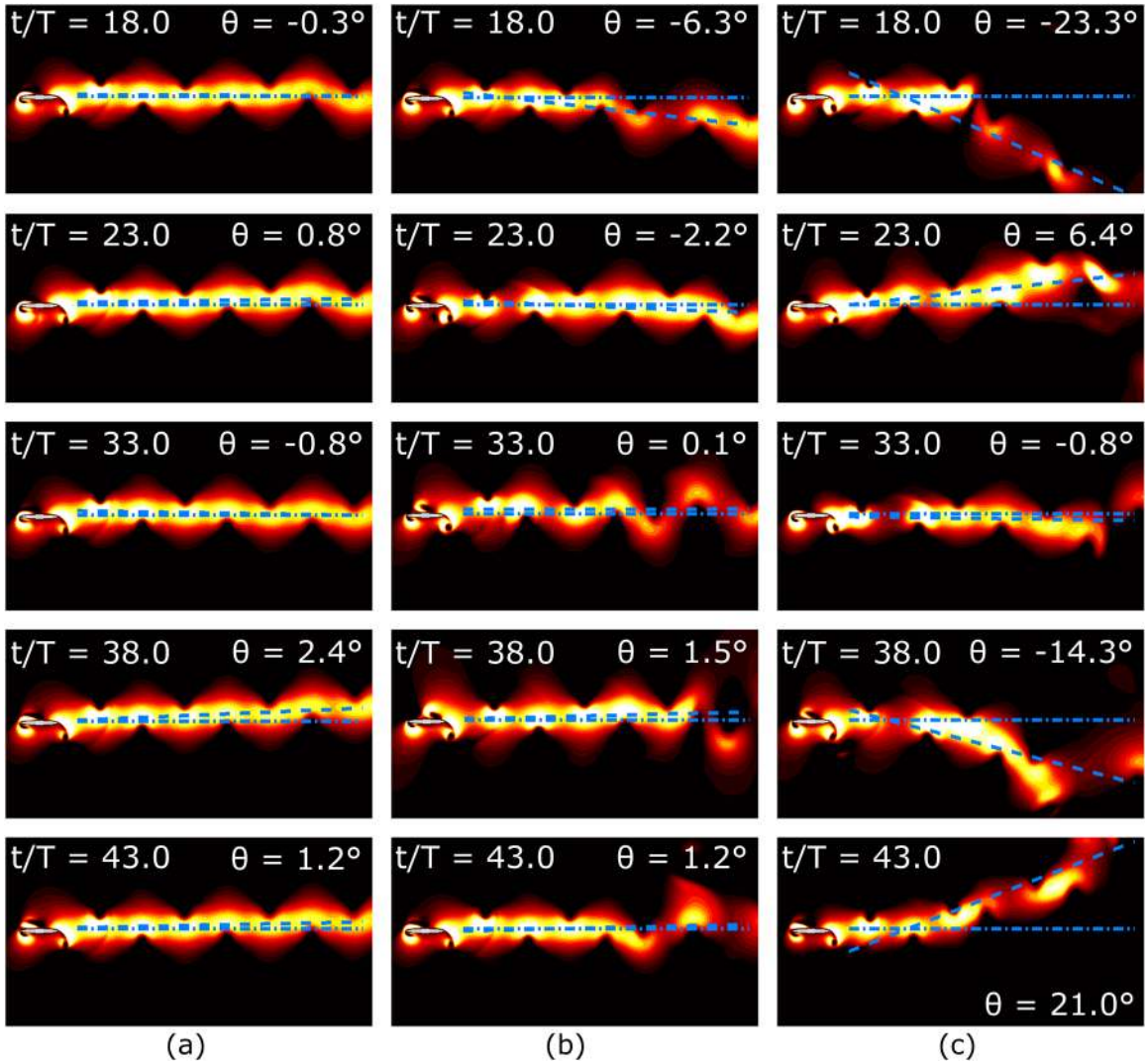

FIG. 14. At κh = 1.5, comparison of deflection angles for (a) constant inflow, (b) long time-scaled input, and (c) short time-scaled input.

trigger for jet-switching. The locations of the cores of **A**, **B**, and **C** are presented in Fig. 16 at the end of 40 consecutive cycles. While the cores shift only marginally during quasi-periodicity under the uniform inflow, they get scattered significantly under the fluctuating inflows and much more so for the short time-scaled case. This eventually results in prominent jet-switching. The variance values associated with the scatter of the vortex cores are estimated to substantiate this claim in an quantitative manner. For the short time-scaled case, the variances of the core locations of **A**, **B**, and **C** increase to 0.21, 0.43, and 0.62, respectively, from negligibly small values of the uniform input case (see Fig. 16).

To understand the switching frequency behavior, three different wake patterns are schematically presented that are observed over the entire simulation period (see Fig. 17). Only one complete switching (D–U–D) is seen for the deterministic inflow condition [see Fig. 17(a)]. On the other hand, multiple (three to four) complete switchings take place for the fluctuating cases. The switching pattern is very abrupt in the case of long time-scaled input with low deflection angles [Fig. 17(b)]. Whereas sustained jet-switching associated with higher deflection angles are observed in the case of short time-scaled input [see Fig. 17(c)].

It is further observed that at κh substantially lower than unity, fluctuating inflows generate only random perturbations of the organized wake but are not able to trigger wake deflection or switching. We conjecture that, in such κh regimes, the strength of the shed vortices is weak and they diffuse fast. Even though the distances between the vortices change due to fluctuations, they diffuse quickly before forming any symmetry breaking couple. Hence, no jet-switching is

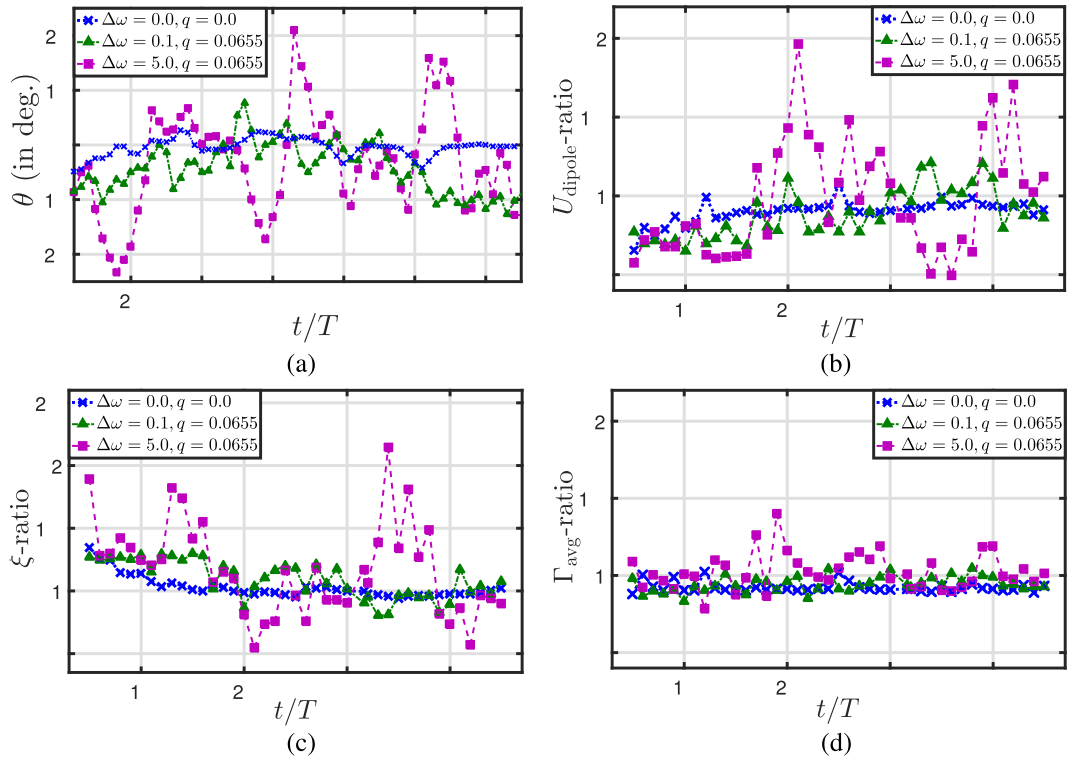

FIG. 15. At κh = 1.5, variation in (a) deflection angle, (b) dipole velocity ratio, (c) distance ratio, and (d) circulation ration for the vortex couples **A**–**B** to **B**–**C** for different inflow conditions.

observed at a very low κh range even in the presence of input perturbations. These results have not been included here for the sake of brevity.

It should be noted that, for different realizations of the input fluctuations, the stay duration of a deflected wake in the upward or downward state and the magnitude of θ might not be exactly repeatable. However, the underlying dynamics and the threshold limit of κh for switching should remain unchanged in a qualitative sense. Even if the quantitative measures might get altered for different realizations, the advancement of switching and its mechanism should

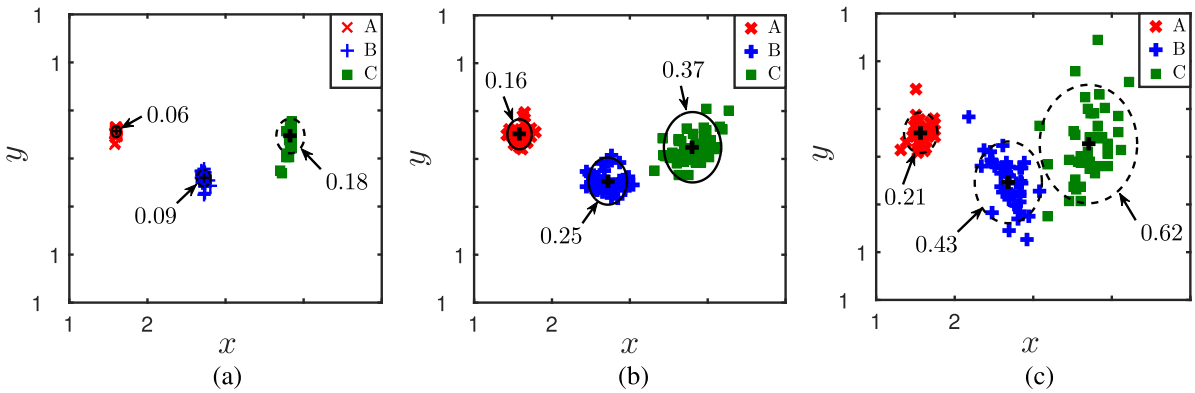

FIG. 16. At κh = 1.50, locations of the vortex core centers of the first three vortices in the wake for (a) constant inflow, (b) long time-scaled input, and (c) short time-scaled input.

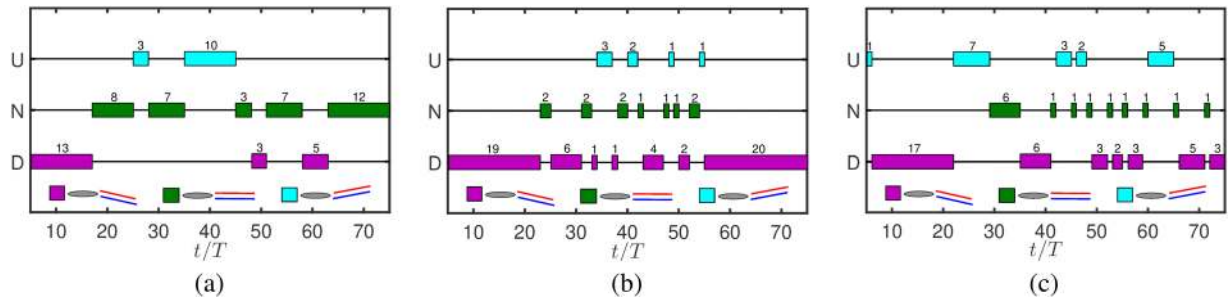

FIG. 17. At κh = 1.5, interval of cycles spent in different deflection modes during jet-switching for (a) constant inflow, (b) long time-scaled input, and (c) short tie-scaled input. Here, U: upward deflected wake; D: downward deflected wake; and N: no deflection.

not get affected. This is, of course, true only if the correlation length of the fluctuation does not change.

VI. VORTEX INTERACTION MECHANISMS

The near-field vortex interactions that lead to jet-switching and invoke changes under fluctuating inputs, such as manifesting higher deflection angles, are examined in this section. Since the effects of inflow fluctuations are more prominent at κh = 1.5, this case alone is discussed.

The formation of symmetry breaking couples plays an important role behind the jet-switching mechanism for a uniform inflow. The associated quasi-periodic movements of the near-wake vortices result in alternate pairing and alternate dominance of the upward and downward deflecting couples. This mechanism does not change significantly for the long time-scaled input too. However, the shed

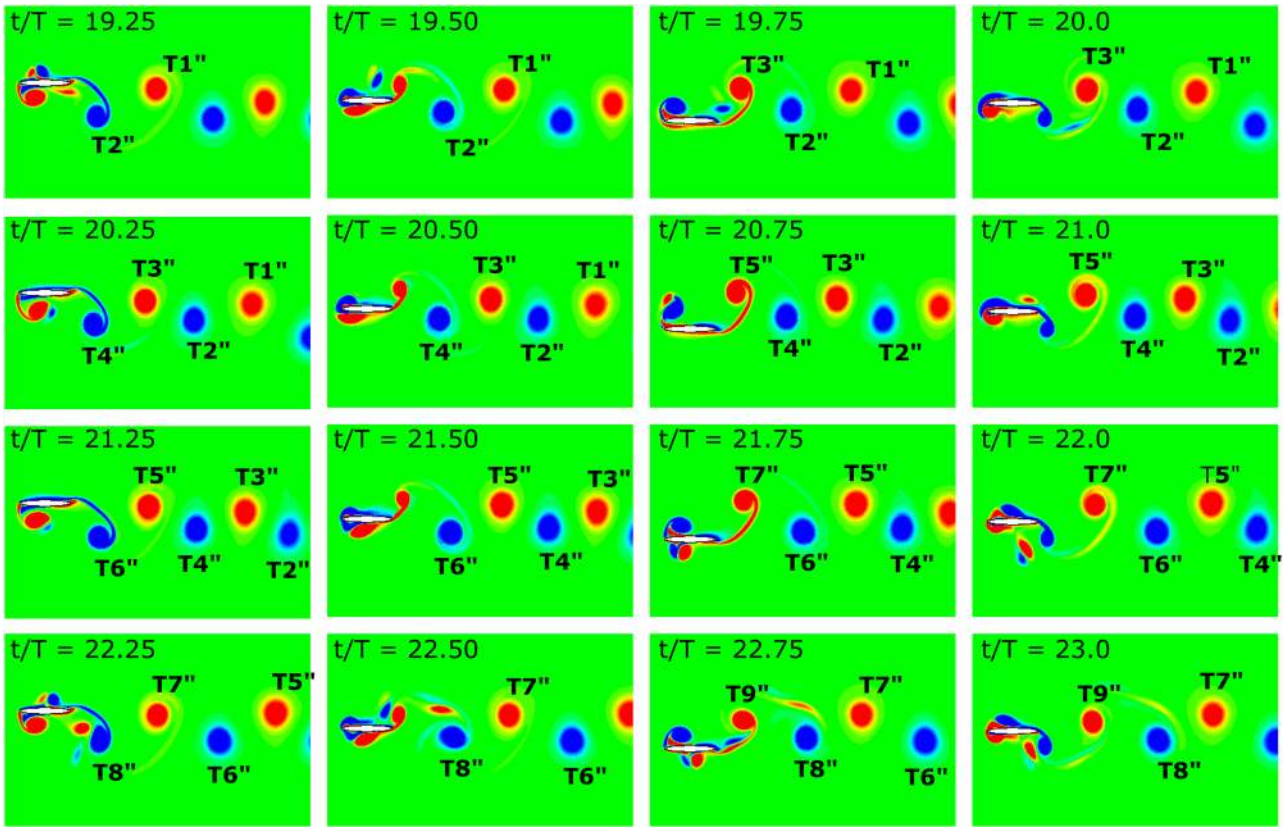

FIG. 18. At κh = 1.5, instantaneous vorticity contours during 20th to 23rd cycles for the long time-scaled input.

vortices do convect with variable speeds during different plunging cycles, and the distances between them change in a random manner. The distances also change by larger extents compared to the uniform inflow case. This phenomenon has already been pointed out through the quantitative measures in Secs. IV–V. The chronology of vortex interactions is presented for four consecutive cycles in Fig. 18 for the long time-scaled input. The distance between two consecutively shed TEVs, **T1**″ and **T2**″, is seen to increase, while the newly shed **T3**″ moves closer to **T2**″ (see for t/T = 19.75–20.0). Consequently, the upward deflecting effect of couple **T3**″–**T2**″ (similar to upward deflecting couple **A**–**B**) becomes dominant. This tries to deflect the mean jet-flow upward. As time progresses, in the earlier part of the 23rd cycle, the stream-wise velocity of the flow becomes higher and carries **T8**″ away from **T9**″, while it moves closer to **T7**″ during t/T = 22.50–23.0. Thus, the downward deflecting tendency of the **T8**″–**T7**″ couple wins over the upward deflecting tendency of **T9**″–**T8**″, causing the mean wake to deflect in the downward direction in the subsequent time. Here, **T2**″ or **T8**″ is nothing but the trailing-vortex **B** according to the description given in Sec. III. At t/T = 20.0, **B** (**T2**″) and **A** (**T3**″) come closer to form the dominant upward deflecting couple, whereas at t/T = 23.0, **B** (**T8**″) moves closer to **C** (**T7**″) to form the dominant downward deflecting couple, thus resulting in jet-switching. It is to be noted that the LEV has no significant role to play behind the jet-switching phenomenon here as switching takes place through an alternate pairing process of shed TEVs, as is also reported for the far-wake switch by Wei and Zheng.[18]

In the case of short time-scaled input, the LEV separation behavior and the subsequent vortex interactions get considerably altered between different cycles as the foil experiences strong unsteady inflow fluctuation, unlike the uniform or long time-scaled cases. It is seen that in some of the cycles, the LEV takes part in switching by randomly interacting with the TEVs, thus contributing directly to the formation of the symmetry breaking couples. In such situations, instead of an individual vortex, a strong vortex couple is shed from the trailing-edge in a random fashion. This trailing couple enhances the asymmetry in the flow-field causing the wake to deflect more in the downward or in the upward direction, thus increasing the deflection angle. In order to demonstrate this, details of the near-field activities during the 19th to 22nd cycles and during the 32nd to 35th cycles are presented in Figs. 19 and 20, respectively. These typical cycles are chosen to mark the instances of the formation of both upward (19th to 22nd cycles) and downward (32nd to 35th cycles) deflecting wakes.

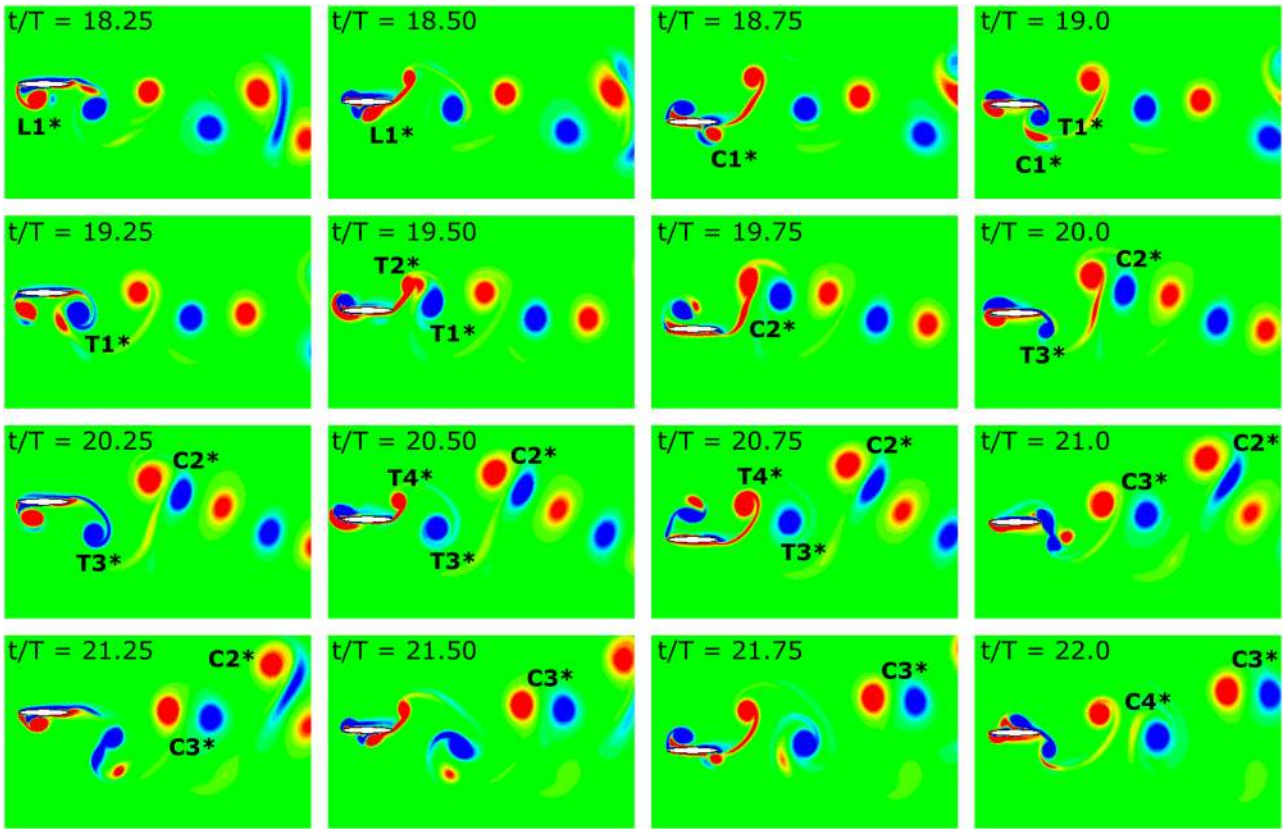

FIG. 19. At κh = 1.5, instantaneous vorticity contours during 19th to 22nd cycles for the short time-scaled input.

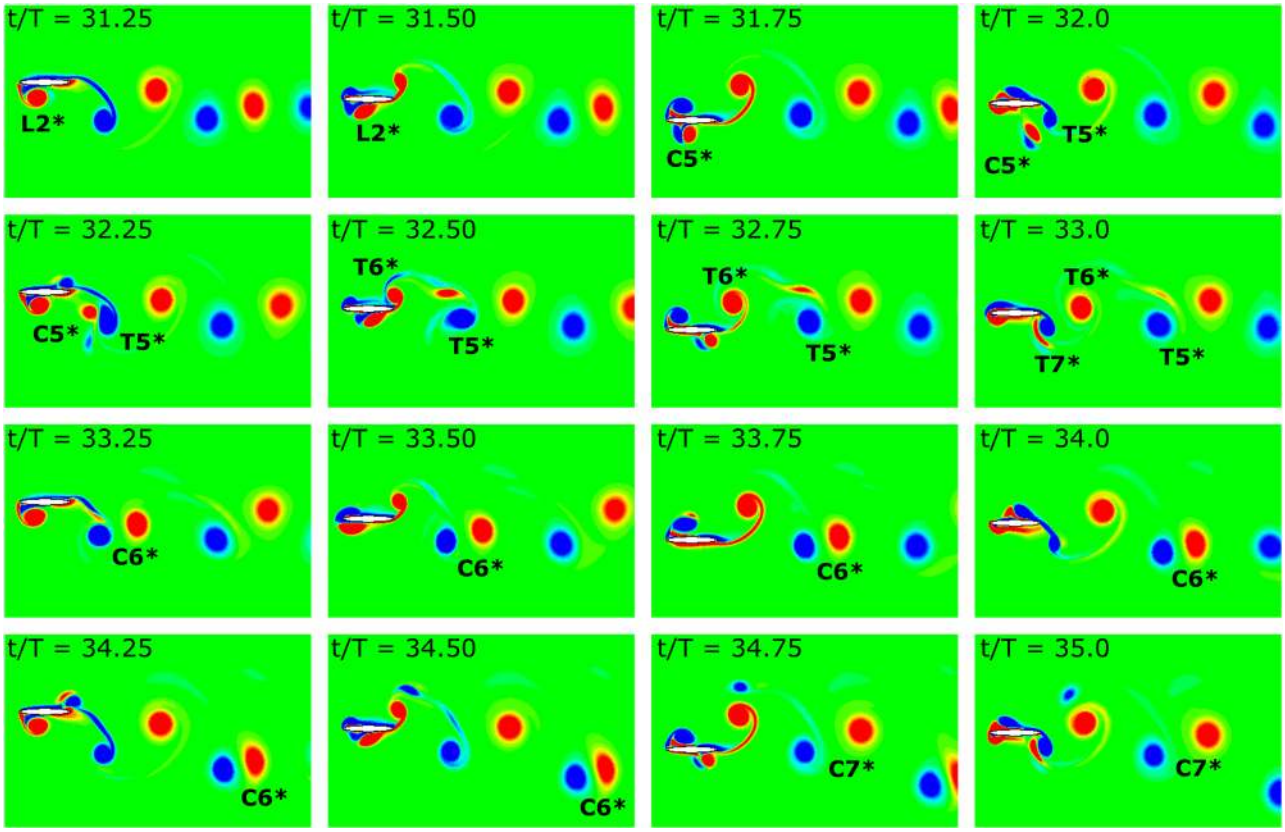

FIG. 20. At κh = 1.5, instantaneous vorticity contours during 32nd to 35th cycles for the short time-scaled input.

In Fig. 19, LEV **L1*** is seen to get developed and stay close to the body around t/T = 18.25–18.50 (Fig. 19); it subsequently forms a couple **C1*** with a CW counterpart fed by the shear layer, which later interacts with a nascent TEV **T1*** (t/T = 18.75–19.0 Fig. 19). **T1*** does not shed away from the trailing-edge but stays close to the foil. During the first half of the 20th cycle, the CCW part of **C1*** merges with the immediate CCW TEV **T2*** (at t/T = 19.25, Fig. 19). Counter-rotating **T1*** and **T2*** pair with each other to form couple **C2***, which moves upward with its self-induced velocity. It entrains the fluid behind it to move toward the same direction and the mean flow in the wake gets deflected, forcing the subsequent TEVs to follow the same upward path. During the 21st cycle, TEVs **T3*** and **T4*** form a couple **C3***, which follows the same path as that of **C2***. Similar trailing-wake behavior is seen in the 22nd cycle as well. In this manner, the downward deflected wake during the 18th cycle with $\theta = -23.3^\circ$ switches to an upward deflected wake with $\theta = 6.4^\circ$ in the 23rd cycle.

Next, transition of an upward deflecting street back to a downward deflecting one is displayed in Fig. 20. The chronology of the near-field events from 32nd to 35th cycles is in focus here, under the same short time-scaled input. It is seen that couple **C5*** (formed from LEV **L2***) undergoes a head-on collision with immediate TEV **T5***, pushing it far away from the trailing-edge (t/T = 31.75–32.75). The CW TEV **T5*** does not form any couple with subsequent CCW **T6*** and sheds away in the wake. Instead, **T6*** forms couple **C6*** with the next CW TEV **T7*** (t/T = 33.0–33.25). **C6*** traverses in the downward direction due to the self-induced velocity causing the mean flow to deflect downward. The same trend is followed by subsequent couple **C7*** in the next cycle. Hence, the upward deflected wake during the 28th cycle with $\theta = 6.7^\circ$ switches to an downward deflected wake with $\theta = -14.3^\circ$ in the 38th cycle through the transition discussed above.

It should be noted here that the formation of couples such as **C1*** and **C5***, and the considerable interactions of the TEVs that are observed here were not seen in the uniform inflow case. For the latter, only a mild-switching took place due to the alternate pairing mechanism triggered by the quasi-periodic movement of the vortices. In contrast, the stochastic inflow induces different LEV formations and influences their subsequent interactions with the TEVs in different flapping cycles.

For uniform and long time-scaled input, evidently only the TEVs take part in the vortex pairing process. However, for the short time-scaled case, the LEVs are seen to play an important role too, as in some of the cycles, the random shedding of the LEV and the consequent LEV–TEV interactions contribute directly to the formation of the symmetry breaking couples. Frequent formation of

couples (such as **C1*** and **C5***) and their interactions enhance the upward/downward deflection process in the way discussed above. Thus, under fluctuating inflows, jet-switching becomes much more prominent with noticeably higher deflection angles and rates of switching. Note that only two such switching instances were presented in this section for the sake of brevity, though it continues to occur at the trailing-edge as time progresses. A continuous temporal evolution of the wake and more details on the LEV behavior under different inflow conditions have been provided in the supplementary material.

VII. CONCLUSIONS

The effect of stochastic input fluctuations on qualitatively distinct trailing-wake patterns of a harmonically plunging foil, involving wake deflection and jet-switching, was investigated in the present study using an IBM-based in-house flow solver. The fluctuating inflow was modeled as an Ornstein–Uhlenbeck process and was incorporated under the inlet boundary condition of the solver. The results for two different κh values were presented, and the mechanisms of wake deflection and jet-switching have been investigated. In the absence of fluctuating inflows, at $\kappa h = 1.0$, the trailing-wake exhibited a periodic reverse Kármán wake with a mild deflection, whereas at $\kappa h = 1.5$, a weak jet-switching phenomenon was observed. The latter was shown to be the result of the quasi-periodic dynamics of the wake vortices. The presence of fluctuating inflows accelerated the switching process that resulted in an advancement of the onset of the jet-switching regime. In addition, the switching became considerably rapid with very high deflection angles depending on the timescales of the fluctuations.

The near-field flow topologies associated with each scenario were studied in detail, and the key mechanisms behind the advancement of the jet-switching onset were identified in terms of various quantitative measures. The change in the distances between the main vortex structures present in the near-wake was found to be one of the most crucial measures associated with the appearance of jet-switching in the wake. It can mark an upward or a downward deflecting couple to be dominant over the other, and consequently, the entire trailing-wake deflects in the direction of the dominant couple. It was found that quasi-periodicity or stochastic perturbations can be instrumental in influencing the inter-gap distances. Random movements of the vortices created under stochastic inflows were responsible for the frequent formation of upward and downward deflecting couples that could eventually drag the fluid behind it, forcing the wake to deflect in their directions. Furthermore, short time-scaled fluctuations also induced qualitatively different LEV separation patterns in different flapping cycles at $\kappa h = 1.5$. This instigated random interactions of the LEVs with TEVs from time to time and resulted in the shedding of couples instead of individual vortices seen otherwise. Thus, the LEVs contributed to the formation of symmetry breaking couples and provided an additional impetus for jet-switching.

SUPPLEMENTARY MATERIAL

See the supplementary material for more details on the LEV behavior and the continuous temporal evolution of the flow-field under the three different inflow conditions.

DATA AVAILABILITY

The data that support the findings of this study are available from the corresponding author upon reasonable request.

REFERENCES

[1] M. F. Platzer, K. D. Jones, J. Young, and J. C. S. Lai, "Flapping wing aerodynamics: Progress and challenges," AIAA J. **46**, 2136–2149 (2008).
[2] I. Gursul and D. Cleaver, "Plunging oscillations of airfoils and wings: Progress, opportunities, and challenges," AIAA J. **57**, 3648–3665 (2019).
[3] S. Watkins, J. Milbank, B. J. Loxton, and W. H. Melbourne, "Atmospheric winds and their implications for microair vehicles," AIAA J. **44**, 2591–2600 (2006).
[4] P. Chirarattananon, Y. Chen, E. F. Helbling, K. Y. Ma, R. Cheng, and R. J. Wood, "Dynamics and flight control of a flapping-wing robotic insect in the presence of wind gusts," Interface Focus **7**, 20160080 (2017).
[5] M. Jones and N. Yamaleev, "The effect of a gust on the flapping wing performance," in *50th AIAA Aerospace Sciences Meeting Including the New Horizons Forum and Aerospace Exposition* (AIAA, 2012), p. 1080.
[6] R. Prater and Y. Lian, "Aerodynamic response of stationary and flapping wings in oscillatory low Reynolds number flows," in *50th AIAA Aerospace Sciences Meeting Including the New Horizons Forum and Aerospace Exposition* (AIAA, 2012), p. 418.
[7] K. Gharali and D. A. Johnson, "Dynamic stall simulation of a pitching airfoil under unsteady freestream velocity," J. Fluids Struct. **42**, 228–244 (2013).
[8] M. M. De, J. S. Mathur, and S. Vengadesan, "Simulation of flapping wings subjected to gusty inflow," Aeronaut. J. **123**, 1170–1192 (2019).
[9] M. M. Koochesfahani, "Vortical patterns in the wake of an oscillating airfoil," AIAA J. **27**, 1200–1205 (1989).
[10] K. D. Jones, C. M. Dohring, and M. F. Platzer, "Experimental and computational investigation of the Knoller–Betz effect," AIAA J. **36**(7), 1240 (1998).
[11] J. C. S. Lai and M. F. Platzer, "Jet characteristics of a plunging airfoil," AIAA J. **37**, 1529–1537 (1999).
[12] R. Godoy-Diana, C. Marais, J.-L. Aider, and J. E. Wesfreid, "A model for the symmetry breaking of the reverse Bénard-von Kármán vortex street produced by a flapping foil," J. Fluid Mech. **622**, 23–32 (2009).
[13] M. Yu, H. Hu, and Z. Wang, "Experimental and numerical investigations on the asymmetric wake vortex structures of an oscillating airfoil," in *50th AIAA Aerospace Sciences Meeting Including the New Horizons Forum and Aerospace Exposition* (AIAA, 2012), p. 299.
[14] Z. C. Zheng and Z. Wei, "Study of mechanisms and factors that influence the formation of vortical wake of a heaving airfoil," Phys. Fluids **24**, 103601 (2012).
[15] S. Heathcote and I. Gursul, "Jet switching phenomenon for a periodically plunging airfoil," Phys. Fluids **19**, 027104 (2007).
[16] S. Y. Shinde and J. H. Arakeri, "Jet meandering by a foil pitching in quiescent fluid," Phys. Fluids **25**, 041701 (2013).
[17] G. C. Lewin and H. Haj-Hariri, "Modelling thrust generation of a two-dimensional heaving airfoil in a viscous flow," J. Fluid Mech. **492**, 339–362 (2003).
[18] Z. Wei and Z. C. Zheng, "Mechanisms of wake deflection angle change behind a heaving airfoil," J. Fluids Struct. **48**, 1–13 (2014).
[19] J. Kim, D. Kim, and H. Choi, "An immersed-boundary finite-volume method for simulations of flow in complex geometries," J. Comput. Phys. **171**, 132–150 (2001).
[20] D. Majumdar, C. Bose, and S. Sarkar, "Capturing the dynamical transitions in the flow-field of a flapping foil using immersed boundary method," J. Fluids Struct. **95**, 102999 (2020).
[21] R. Graham and A. Schenzle, "Stabilization by multiplicative noise," Phys. Rev. A **26**, 1676 (1982).
[22] D. T. Gillespie, "Exact numerical simulation of the Ornstein–Uhlenbeck process and its integral," Phys. Rev. E **54**, 2084 (1996).
[23] D. J. Higham, "An algorithmic introduction to numerical simulation of stochastic differential equations," SIAM Rev. **43**, 525–546 (2001).
[24] R. C. Hilborn *et al.*, *Chaos and Nonlinear Dynamics: An Introduction for Scientists and Engineers* (Oxford University Press on Demand, 2000).